Energy Conversion and Management 280 (2023) 116816

Contents lists available at ScienceDirect

Energy Conversion and Management

journal homepage: www.elsevier.com/locate/enconman

Green ammonia production *via* the integration of a solid oxide electrolyser and a Haber-Bosch loop with a series of solid electrolyte oxygen pumps

Duncan A. Nowicki *, Gerry D. Agnew, John T.S. Irvine

School of Chemistry, University of St Andrews, North Haugh, St Andrews, Fife KY16 9ST, UK

ARTICLE INFO

Keywords:
Solid oxide electrolysis
Ammonia
Solid electrolyte oxygen pump
Hydrogen

ABSTRACT

A conceptual design for a small-scale green ammonia plant is presented in which ammonia synthesis was realised *via* a Haber-Bosch loop using hydrogen produced by a solid oxide electrolyser and nitrogen purified from air with a series of solid electrolyte oxygen pumps. The system operated with an energetic efficiency of 52.12%, very close to a cryogenic ASU reference system where an efficiency of 52.89% was achieved. The specific energy consumption was 9.94 kWh/kgNH_3. Whilst these were encouraging results, opportunities exist to improve system design further. For example, greater heat integration could allow for steam required by the electrolyser to be raised using waste heat from the series of oxygen pumps.

1. Introduction

In their 2014 report, the Intergovernmental Panel on Climate Change projected that greenhouse gases could become so abundant in the atmosphere that by the year 2100 the global mean surface temperature of the Earth may be more than 4 °C warmer than it was during the pre-industrial era [1]. Consequently, immediate action is required to reduce the magnitude of anthropogenic greenhouse gas emissions if catastrophic disruption to the Earth's climate system is to be avoided.

Ammonia (NH_3) is an important industrial chemical, with approximately 176 million tonnes produced annually primarily for use in agriculture as a fertilizer [2]. Presently, ammonia is produced on a large-scale *via* the Haber-Bosch process where hydrogen is reacted with nitrogen at high temperature and pressure in the presence of an iron-based catalyst. Whereas the nitrogen used in this process can be obtained from air, the required hydrogen is usually derived from fossil fuels (e.g. *via* the steam reforming of natural gas or the gasification of coal), with approximately 2.6 tonnes of CO_2 equivalent released per tonne of product NH_3 [3]. Although the resultant carbon dioxide could be captured by deploying technologies such as the coke-oven gas chemical looping process reported by [4] and then either stored [5] or utilised in the production of useful materials [6–8], additional capital and operating costs would be incurred [9,10]. Therefore, it is self-evident that decarbonising NH_3 production must constitute a key element of any serious climate strategy.

Various low-carbon hydrogen production methods including thermochemical water splitting, photoelectrochemical water splitting, and biomass fermentation have been demonstrated [11,12]. However, due to issues such as low H_2 production rates and conversion efficiencies biomass gasification and water electrolysis are currently the only viable options given the required scale of implementation. Zhang *et al.* [33] investigated two low-carbon ammonia production processes, where the H_2 was obtained either by biomass gasification or steam electrolysis using a solid oxide electrolyser (SOE) and the N_2 was supplied by an air separation unit (ASU), and compared these to a conventional ammonia plant based on the steam reforming of methane (SMR). Whilst both required multiple steps (reforming, water–gas shift, CO_2 removal and methanation) to prepare the pure stream of hydrogen, the biomass-based approach operated much less efficiently (44%) than the SMR plant (61%) as the particulars of the feedstock meant that more CO_2 had to be removed in order to produce the same quantity of ammonia. Conversely, the SOE-based system achieved an energetic efficiency above 74% thanks to optimal placement of steam cycles for heat recovery. Additionally, the plant design of this process was markedly less complex as the only inputs were air, water and electricity which allowed for unreacted steam to simply be condensed out. The levelized production cost of the biomass case ($450/ton) was relatively close to that of the SMR case ($374/ton), whereas the SOE approach had a much greater production cost of $544/ton due to high stack and electricity costs. However, the authors did acknowledge that the economic competitiveness of this approach will likely improve as production costs fall and renewable energy gains wider deployment. The viability of deploying

* Corresponding author.
E-mail addresses: dan1@st-andrews.ac.uk (D.A. Nowicki), ga58@st-andrews.ac.uk (G.D. Agnew), jtsi@st-andrews.ac.uk (J.T.S. Irvine).

https://doi.org/10.1016/j.enconman.2023.116816
Received 27 October 2022; Received in revised form 30 January 2023; Accepted 11 February 2023
Available online 19 February 2023

SOEs for preparing the hydrogen for ammonia synthesis has also been compared to other types of electrolysers. In a modelling study, Frattini *et al.* [13] integrated a low-temperature electrolyser operating at 80 °C and 30 bar with a pressure-swing adsorption based ASU (room temperature and 30 bar) and realised a specific energy consumption of 14.36 kWh/kgNH_3. Cinti *et al.* [14] reported a specific energy consumption of 14.25 kWh/kgNH_3 for a similar system, close to the 14.59 kWh/kgNH_3 they achieved using a natural gas reforming based route. The group were also able to reduce the specific energy consumption of ammonia production to 8.30 kWh/kgNH_3 by replacing the low-temperature electrolyser with a SOE operating at 650 °C and 1 bar. This significant drop was attributed to the combination of reduced electrolyser electrical demand thanks to the higher operating temperature (falling from 13.59 kWh/kgNH_3 to 6.50 kWh/kgNH_3) as well as the opportunity to recover waste heat from the Haber-Bosch reactor which allowed for SOE thermal equilibrium to be maintained without external heat input. Moreover, in both electrolysis cases the authors observed an improvement in the performance of the Haber-Bosch loop relative to the reforming route due to the absence of inert species such as O_2, CO and CO_2.

Whilst the benefits of producing ammonia *via* a paired SOE and ASU are clear, current air separation units are expensive at small scale [2] which will likely prevent the deployment of decentralised NH_3 production facilities in rural or remote locations. The aim of this work was therefore to investigate whether this limitation could feasibly be overcome by performing a modelling study in which a cryogenic ASU was substituted by a series of Solid Electrolyte Oxygen Pumps (SEOPs), which possess a degree of modularity analogous to that of an SOE. In the first section, relevant theory pertinent to the Haber-Bosch process, SOEs and SEOPs is presented. This is followed by a detailed description of the modelling of the novel system, as well as the development of a reference system in which the nitrogen required for ammonia synthesis was produced using a cryogenic ASU. Finally, the main results obtained from these models are presented and analysed.

2. Methods

2.1. Background theory

2.1.1. Overview of ammonia synthesis

On an industrial scale, ammonia is produced *via* the Haber-Bosch process where the constituent elements hydrogen and nitrogen are reacted at high temperature and pressure in the presence of an iron-based catalyst in accordance with the reaction shown in Equation (1):

$$N_2 + 3H_2 \rightleftharpoons 2NH_3 \quad \Delta H^\circ = -91.8 \ kJ/mol \tag{1}$$

Synthesis is usually performed at temperatures of 350–500 °C and pressures of 150–300 bar [15]. Whilst the exothermic nature of the reaction would dictate that lower temperatures are preferable, this temperature range allows for an acceptable balance between equilibrium ammonia yield and rate of reaction to be achieved. However, even under these compromise conditions, conversion remains low at approximately 15–35% per pass [15,16]. Additionally, oxygen-containing species such as O_2, H_2O, CO and CO_2 are known Haber-Bosch catalyst poisons [17]. Therefore, a complex plant design is usually required to maximise both yield and process efficiency.

2.1.2. Solid oxide electrolysers (SOEs)

Solid oxide electrolysers (SOEs) can produce H_2 *via* the electrolysis of steam. A typical SOE consists of a cathode, a dense oxide-ion conducting electrolyte material and an anode and can essentially be conceived of as a solid oxide fuel cell (SOFC) run in reverse i.e. whereas a SOFC uses hydrogen to produce electricity, a SOE uses electricity to produce hydrogen. The operating principle of a SOE steam electrolyser is shown in Fig. 1. Steam enters on the cathode-side of the cell where it reacts with

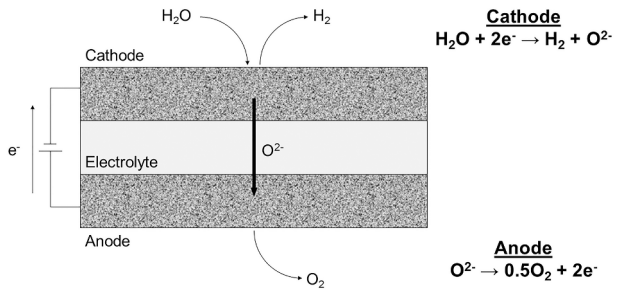

Fig. 1. Operating principle of a solid oxide electrolyser (SOE) for the production of hydrogen from steam. Air is usually fed into the anode channel to avoid the dangerous build-up of oxygen gas but this was not included here.

electrons provided by an external power source and is split into hydrogen and oxide (O^{2-}) ions. If the electricity required to power the device were to be generated by renewable sources such as wind or solar power, 'green hydrogen' could be produced with no release of greenhouse gases. These ions then migrate through the dense electrolyte layer to the anode side of the cell where they are oxidised to form oxygen gas, which exits *via* the anode outlet. To avoid the dangerous build-up of oxygen gas, air is usually fed into the anode channel during operation although this does not react and so was not included in Fig. 1. The respective reactions at the cathode and anode are shown in Equation (2) and Equation (3), with the overall cell reaction shown in Equation (4):

$$\text{Cathode half-cell}: H_2O + 2e^- \rightarrow H_2 + O^{2-} \tag{2}$$

$$\text{Anode half-cell}: O^{2-} \rightarrow 0.5O_2 + 2e^- \tag{3}$$

$$\text{Overall}: H_2O \rightarrow H_2 + 0.5O_2 \tag{4}$$

The energy required for the overall reaction, ΔH, is well known to consist of two terms: Gibbs free energy change (ΔG) and reaction entropy change multiplied by temperature ($T\Delta S$), Equation (5):

$$\Delta H = \Delta G - T\Delta S \tag{5}$$

Whereas $T\Delta S$ must be supplied to the cell as heat, ΔG must be provided as electrical energy and therefore can be related to the equilibrium potential (i.e. the open-circuit voltage) of the cell by Equation (6):

$$E_{REV} = \frac{\Delta G}{nF} \tag{6}$$

where E_{REV} is the equilibrium potential (V), ΔG is the Gibbs free energy change (kJ/mol), n is the number of moles of electrons transferred per mole of reaction (each mole of steam requires two moles of electrons and so $n = 2$) and F is Faraday's constant (96485 C/mol). From the fundamental definition of Gibbs free energy, the equilibrium potential can also be expressed in terms of the partial pressures of the gaseous species involved in the steam decomposition reaction as shown by Equation (7), where E° is the standard potential (V), R is the universal gas constant (J/mol·K), T the SOE operating temperature (K), $P_{H_2,c}$ and $P_{H_2O,c}$ the partial pressures of hydrogen and steam respectively on the cathode-side of the SOE (bar) and $P_{O_2,a}$ the partial pressure of oxygen on the anode-side (bar):

$$E_{REV} = \mathrm{E}^\circ + \frac{RT}{nF} ln\left[\frac{P_{H_2,c}\left(P_{O_2,a}\right)^{0.5}}{P_{H_2O,c}}\right] \tag{7}$$

Between 600 and 1200 K, the standard potential can be found using Equation (8):

$$E^\circ = 1.253 - 0.00024516T \tag{8}$$

In practise, a voltage greater than the Nernst potential will be required in order to overcome ohmic, concentration and activation overpotentials. This additional energy will primarily be converted to

heat and thus the magnitude of the applied overpotential will determine whether the electrolyser will operate in either endothermic, exothermic or thermoneutral mode [18]:

- **Endothermic mode:** In this case, less heat is produced by the overpotential than that consumed by the electrolyser ($T\Delta S$); an external heat source is thus required to operate isothermally.
- **Exothermic mode:** A large overpotential generates more heat than is absorbed during the endothermic electrochemical reaction, necessitating heat be removed to maintain a constant temperature across the electrolyser.
- **Thermoneutral mode:** Here, the heat produced by the overpotential is equal to the heat absorbed by the cell and so the SOE temperature will remain constant without any external heat management. The voltage at which this thermoneutral state is realised is related to the enthalpy change associated with the steam decomposition reaction, Equation (9):

$$V_{TN} = \frac{\Delta H}{nF} \tag{9}$$

where E_{TN} is the thermoneutral voltage (V) and ΔH the reaction enthalpy change (kJ/mol). Each of these thermodynamic terms (ΔH, ΔG and $T\Delta S$) is a function of temperature as demonstrated by Fig. 2. Whereas the total energy demand is relatively invariant with increasing temperature, a significant reduction in ΔG is observed, whilst $T\Delta S$ increases. Consequently, the high operating temperatures of SOEs (typically between 650 and 1000 °C) allow them to achieve much higher efficiencies than those possible using alkaline or proton exchange membrane (PEM) electrolysers, which operate at much lower temperatures [19].

2.1.3. Solid electrolyte oxygen pumps (SEOPs)

Solid electrolyte oxygen pumps (SEOPs) are devices similar to SOEs that can separate oxygen from gaseous mixtures by exploiting the ability for oxide ions to move through the dense electrolyte material. Consequently, they can be used to generate the nitrogen required for ammonia synthesis from air. A schematic of a SEOP is shown in Fig. 3. The operating principle is comparable to that of an SOE. At the cathode, oxygen gas is reduced to form oxide ions, which migrate through the electrolyte to the anode where they are oxidised and liberated. Again, air is usually swept on the anode-side of the cell but this was not included in the schematic. Unlike the SOE however, no net endothermic reaction takes place inside the SEOP. Instead, the device acts simply as an oxygen separation membrane, 'pumping' oxygen from cathode to anode under

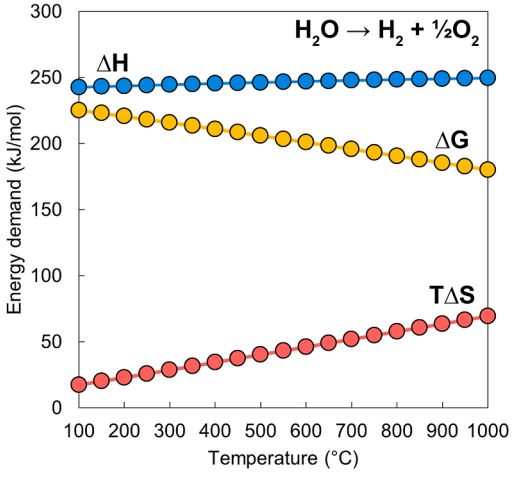

Fig. 2. The variation of ΔH, ΔG, and $T\Delta S$ for steam electrolysis, plotted as a function of temperature between 100 and 1000 °C.

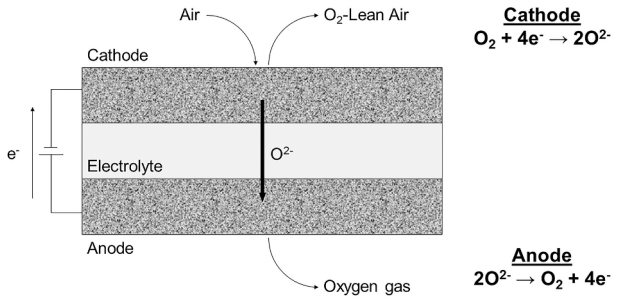

Fig. 3. Schematic of a solid electrolyte oxygen pump (SEOP) separating oxygen from air.

electric load [20]. The equilibrium potential of a given SEOP can be calculated using Equation (10) [21]:

$$E_{REV} = \frac{RT}{nF} ln\left(\frac{P_{O_2,a}}{P_{O_2,c}}\right) \tag{10}$$

Where $P_{O_2,a}$ and $P_{O_2,c}$ are the partial pressures of oxygen at the anode and cathode respectively (bar). Note that here n has a value of four rather than two as for SOE steam electrolysis.

2.2. Process overview & model development

In this section, an outline of the two steady-state plants studied in this work is given as well as a detailed description of the methodology used to model certain unit operations or segments. Simulations were performed with the software package DWSim, using the Peng-Robinson equation of state for physical and chemical calculations. In each case, NH_3 synthesis was realised *via* a Haber-Bosch loop (HBL), with the required hydrogen produced from steam using a ~ 1 MW SOE. The electrolyser operated under identical conditions in each case. Modelling of the Haber-Bosch loop was loosely based on a configuration previously published by Frattini *et al.* [13]. Additionally, in each system a portion of the steam required by the SOE was generated using the waste heat from the exothermic Haber-Bosch Reactor (HBR). The difference between the plants arises in the method used to obtain the N_2 required for ammonia synthesis. In the first system, case A, a series of SEOPs was used whereas in the second plant (case B) an ASU was employed instead. Therefore, each full-system model consisted of three distinct sub-sections: an SOE sub-section responsible for hydrogen generation, another sub-section in which a purified nitrogen stream was produced and a Haber-Bosch sub-section in which ammonia synthesis and purification was realised. Process flow diagrams of the two models are shown in Fig. 4 & Fig. 5.

2.2.1. Process overview

Water is introduced into the system at 1.32 bar by PUMP-01 and pre-heated to 100 °C in HE-01. Evaporation takes place in HEATER-01, which produces superheated steam at 120 °C and 1.26 bar. This is then combined with a small flow of recirculated H_2 (to avoid degradation of the cathode electrode) and the steam raised by the HBR waste heat in MIX-01, heated by the cathode-side product stream in HE-02 and trimmed to the SOE operating temperature in HEATER-03. Note that the steam raised using the HBR waste heat is produced *via* HEATER-02. PUMP-02 feeds liquid water at 25 °C and 1.26 bar to HEATER-02, which heats this to 300 °C. The flow of H_2O sent to PUMP-02 was controlled such that the heat input to HEATER-02 matched that given off by the Haber-Bosch Reactor. On the anode-side of the electrolyser, air (79 mol% N_2, 21 mol% O_2) is circulated to reduce the partial pressure of oxygen. This sweep air is first compressed to 1.29 bar by COMP-01 and then fed through HE-03 and HE-04, where heat is recuperated from the anode-side exhaust stream. The temperature is finally trimmed in HEATER-04 before reaching the SOE. To ensure isothermal operation, the electrolyser was housed inside an electric furnace which provided

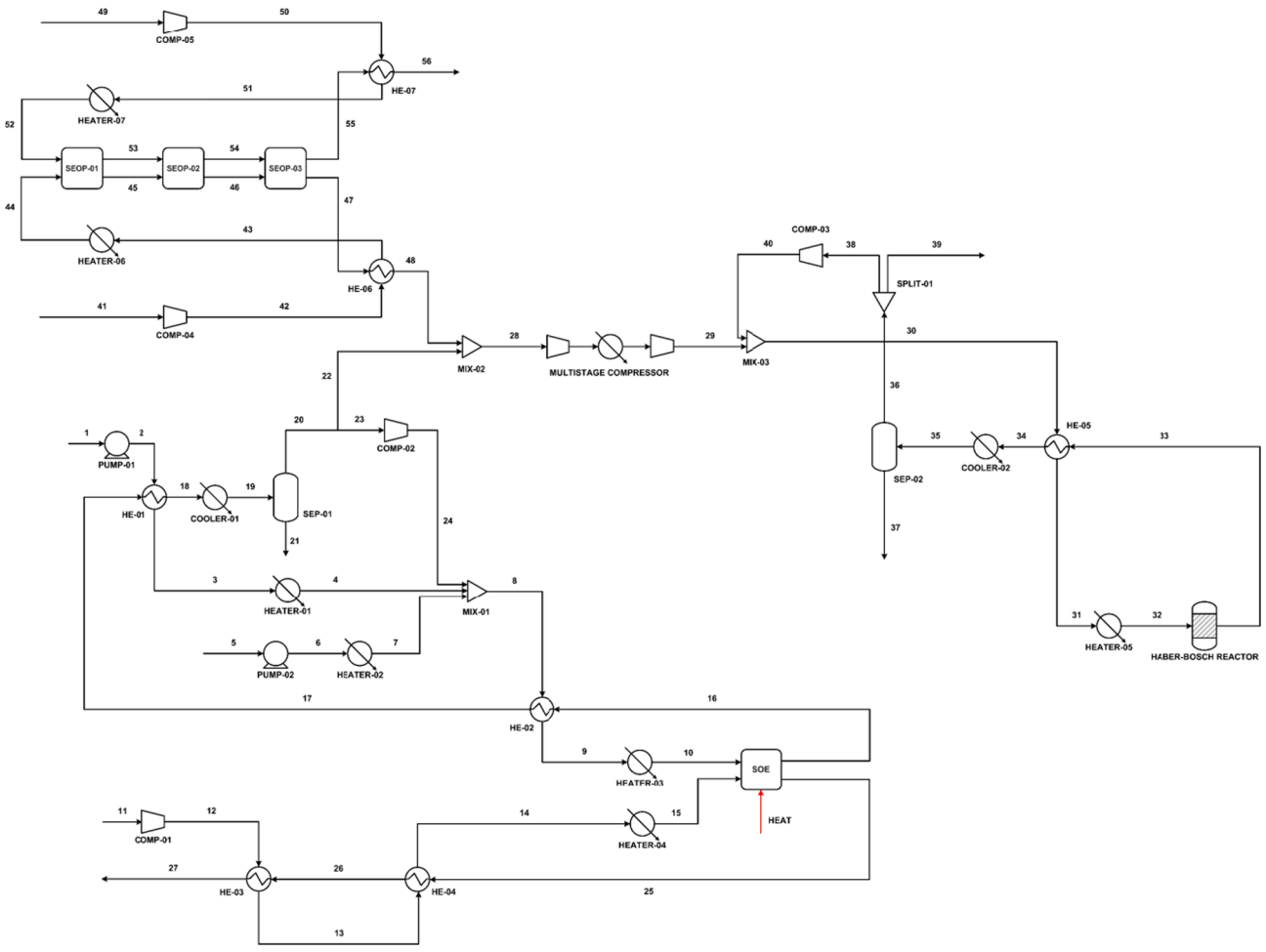

Fig. 4. Process flow diagram of system case A where the purified N_2 stream for ammonia synthesis was produced from air using a series of solid electrolyte oxygen pumps (SEOPs).

heat to the unit to account for the endothermic steam decomposition reaction. After being cooled to 50 °C by the air-fed COOLER-01, water is condensed out from the cathode-side product stream at 25 °C in SEP-01, with a fraction of the resultant vapour recirculated as mentioned previously *via* COMP-02. The quantity of hydrogen recirculated to the SOE was calculated to ensure a cathode inlet composition of 90 mol% H_2O and 10 mol% H_2. The remaining hydrogen is combined with the nitrogen stream produced by either the ASU or the SEOPs in MIX-02; the particulars of N_2 production will be discussed in detail later. The H_2/N_2 feed gas mixture is then passed through a 6-stage compression train to achieve the pressure required for ammonia synthesis, with intercooling to 50 °C between subsequent stages. Then, the compressed H_2/N_2 mixture is combined with the Haber-Bosch recycle (stream 40) before this mixture is heated first in HE-05 by the HBR product stream and then in HEATER-05. After exiting HE-05, the HBR product is further cooled to 50 °C in COOLER-02 before most of the synthesised ammonia is removed in SEP-02, which operates at 5 °C and 150 bar. A portion of the resultant vapour stream (stream 36) is purged from the system *via* SPLIT-01 to prevent the build-up of O_2 and H_2O in the loop; the remainder has its pressure adjusted in COMP-03 to account for the pressure drops associated with the HBL. Finally, the produced ammonia leaves the system as a liquid (stream 37), with a purity of 94.53 mol%.

2.2.2. Model development

The SOE model had to account for several processes including: the cathode-side steam decomposition reaction; the production of oxygen gas at the anode and the mixing of this gas with the sweep air; simulation of electric behaviour; and overall electrolyser energy balance. As a unit operation suitable for the satisfactory simulation of all of these processes is not included as a default in DWSim, a custom Python script model was used instead.

The reactant utilisation equation (Equation (11)), which represents the extent to which reactants are converted into products [22,23], was used to compute the cathode-side material balance:

$$RU = \frac{R_{react}}{R_{in}} = \frac{JA}{nFR_{in}} \tag{11}$$

Where RU is the reactant (i.e. the steam) utilisation factor, R_{react} and R_{in} are the flowrates of steam reacted in and fed to the electrolyser respectively (mol/s), J the applied current density (A/cm^2) and A the active reaction area of the SOE (cm^2). After calculating the flowrate of steam required to be fed to the SOE to achieve a desired RU using the known inputs J and A, R_{react} was calculated and thus the output flowrate of steam (and consequently hydrogen) found. R_{react}, along with the stoichiometry of Equation (4), was also used to evaluate the molar flowrate of oxygen gas produced at the anode. With no reaction to consider however, the anode-side material balance was completed by simply adding this additional oxygen gas to the sweep air fed to the cell. The flowrate of sweep air was set such that the oxygen molar fraction in the anode-side exhaust stream would achieve a desired value.

The operating voltage V (V) was found by summing the Nernst potential (calculated using Equation (7)) and each of the polarization losses as shown by Equation (12), where η_{ohmic} is the ohmic overpotential, $\eta_{conc,c}$ is the concentration overpotential at the cathode, $\eta_{conc,a}$

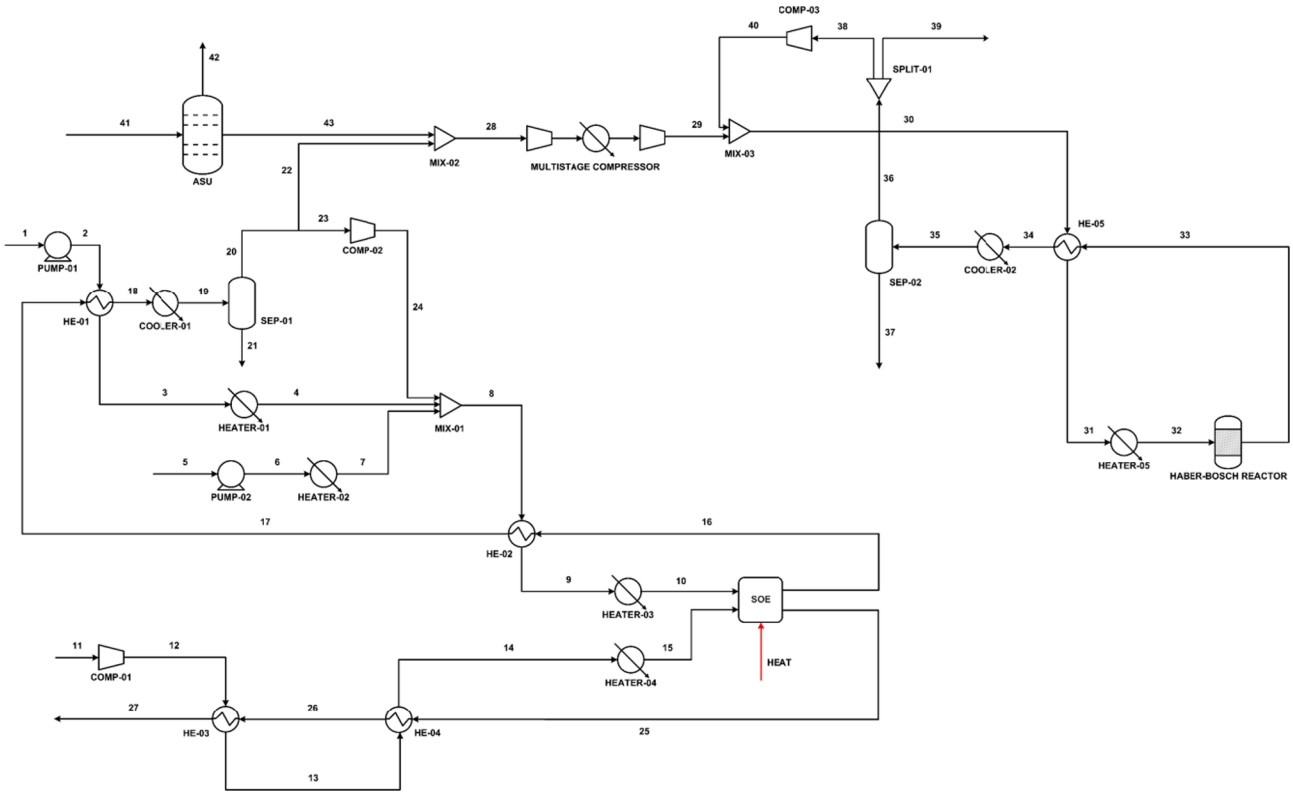

Fig. 5. Process flow diagram of case B, where a cryogenic air separation unit was used to separate from air the N_2 used for ammonia synthesis.

the concentration overpotential at the anode and $\eta_{act,c}$ and $\eta_{act,a}$ the activation overpotentials at the cathode and anode respectively:

$$V = E_{REV} + \eta_{ohmic} + \eta_{conc,c} + \eta_{conc,a} + \eta_{act,c} + \eta_{act,a} \tag{12}$$

The electrical power (kW) consumed by the SOE was found using Equation (13):

$$P = \frac{JAV}{1000} \tag{13}$$

The ohmic overpotential η_{ohmic} (V) is caused by the resistance to flow of ions and electrons through the electrolyte and electrode materials respectively and consequently is dependent on cell configuration and geometry. It obeys Ohm's law and thus was calculated using Equation (14):

$$\eta_{ohmic} = 1E + 4 \cdot J\left(\frac{\tau_c}{\sigma_c} + \frac{\tau_e}{\sigma_e} + \frac{\tau_a}{\sigma_a}\right) \tag{14}$$

Where τ_i and σ_i are the thickness (m) and conductivity ($\Omega^{-1}\cdot m^{-1}$) of each cell component respectively. The ionic conductivity of the electrolyte was found using Equation (15):

$$\sigma_e = 3.32E + 4 \cdot exp\left(-\frac{1.03E + 4}{T}\right) \tag{15}$$

The concentration overpotential at the cathode $\eta_{conc,c}$ and anode $\eta_{conc,a}$ (V) were calculated using Equation (16) and Equation (17) respectively:

$$\eta_{conc,c} = \frac{RT}{nF} ln\left(\frac{P^{TPB}_{H_2,c} P_{H_2O,c}}{P_{H_2,c} P^{TPB}_{H_2O,c}}\right) \tag{16}$$

$$\eta_{conc,a} = \frac{RT}{nF} ln\left[\left(\frac{P^{TPB}_{O_2,a}}{P_{O_2,a}}\right)^{0.5}\right] \tag{17}$$

Here, the subscripts c and a refer to the cathode and anode respectively and the superscript *TPB* the electrode triple-phase boundary where the electrochemical reactions take place. The pressure of H_2O and H_2 at the cathode triple-phase boundary $P^{TPB}_{H_2O,c}$ and $P^{TPB}_{H_2,c}$ (bar) were calculated using Equation (18) and Equation (19) respectively, where D^{eff}_c is the cathode overall effective diffusion coefficient (m^2/s), Equation (20):

$$P^{TPB}_{H_2O,c} = P_{H_2O,c} - \left(\frac{0.1RTJ\tau_c}{D^{eff}_c nF}\right) \tag{18}$$

$$P^{TPB}_{H_2,c} = P_{H_2,c} + \left(\frac{0.1RTJ\tau_c}{D^{eff}_c nF}\right) \tag{19}$$

$$D^{eff}_c = \left(\frac{P_{H_2O,c}}{P_c}\right) D^{eff}_{H_2} + \left(\frac{P_{H_2,c}}{P_c}\right) D^{eff}_{H_2O} \tag{20}$$

Equation (20) shows that the cathode overall effective diffusion coefficient is dependent on the individual effective diffusion coefficients of H_2O and H_2. These can be calculated using Equation (21), accounting for the microstructure of the electrode material itself and the fact that diffusion occurs by both molecular (Equation (22)) and Knudsen diffusion mechanisms (Equation (23)):

$$\frac{1}{D^{eff}_i} = \frac{\zeta}{\varepsilon}\cdot\left(\frac{1}{D_{i-j}} + \frac{1}{D_{k,i}}\right) \tag{21}$$

$$D_{i-j} = \frac{1E - 7T^{1.75}\left(\frac{1}{M_i} + \frac{1}{M_j}\right)^{0.5}}{\frac{P_c}{1.01325}\left[(V_i)^{0.33} + (V_j)^{0.33}\right]^2} \tag{22}$$

$$D_{k,i} = 97 r_p \sqrt{\frac{T}{M_i}} \tag{23}$$

where ζ and ε are the electrode tortuosity and porosity respectively (unitless), D_{ij} is the binary molecular diffusion coefficient (m^2/s) of a gaseous mixture of components i and j, $D_{k,i}$ is the Knudsen diffusion

coefficient of component i (m^2/s), M_i and M_j are the molecular weights of each species (g/mol), V_i and V_j the diffusion volumes of the species (unitless) and r_p the average radius of electrode pores (m).

On the anode-side of the cell, the nitrogen flux was zero as this component was neither consumed nor produced. Therefore, oxygen transported by self-diffusion. For one-dimensional diffusion, the molar flux of oxygen N_{O_2} (mol/cm^2·s) is given by Equation (24), where $D_{O_2}^{eff}$ is the effective diffusion coefficient of oxygen (m^2/s), C_{O_2} the oxygen concentration (mol/m^3) and X_{O_2} the O_2 mole fraction (unitless):

$$N_{O_2} = -D_{O_2}^{eff}\frac{dC_{O_2}}{d\tau_a} + X_{O_2}\delta_{O_2}N_{O_2} \tag{24}$$

Whereas $D_{O_2}^{eff}$ was calculated using Equation (21) (with the binary molecular diffusion coefficient calculated with respect to the mixture of N_2/O_2 fed to the anode), δ_{O_2} was defined by the expression shown in Equation (25) where the effective Knudsen and molecular diffusion coefficients were computed using Equation (26) and Equation (27) respectively:

$$\delta_{O_2} = \frac{D_{O_2,k}^{eff}}{D_{O_2,k}^{eff} + D_{O_2-N_2}^{eff}} \tag{25}$$

$$D_{O_2,k}^{eff} = \frac{\varepsilon}{\zeta}D_{O_2,k} \tag{26}$$

$$D_{O_2-N_2}^{eff} = \frac{\varepsilon}{\zeta}D_{O_2-N_2} \tag{27}$$

It is known that $N_{O_2} = J/nF$ as oxygen is produced at the electrode, $dC_{O_2} = dP_{O_2,a}/RT$ and $X_{O_2} = P_{O_2,a}/P_a$. Note that here n has a value of four. Substituting these definitions into Equation (24) and rearranging gives Equation (28):

$$\frac{dP_{O_2,a}}{\left(\frac{P_a}{\delta_{O_2}} - P_{O_2,a}\right)} = -\frac{0.1J\delta_{O_2}RT}{nFD_{O_2}^{eff}P_a}d\tau_a \tag{28}$$

Integrating this expression with the boundary condition $P_{O_2,a}^{TPB} = P_{O_2,a}$ at the electrode surface yields Equation (29), which allows for the partial pressure of oxygen at the anode triple-phase boundary (bar) to be found:

$$P_{O_2,a}^{TPB} = \frac{P_a}{\delta_{O_2}} - \left[\left(\frac{P_a}{\delta_{O_2}} - P_{O_2,a}\right)exp\left(-\frac{0.1J\delta_{O_2}RT\tau_a}{nFD_{O_2}^{eff}P_a}\right)\right] \tag{29}$$

The activation overpotential associated with each SOE electrode $\eta_{act,i}$ (V) is commonly modelled using the well-known Butler-Volmer equation, Equation (30):

$$J = 1E-4 \bullet J_{o,i}\left[exp\left(\frac{\alpha nF\eta_{act,i}}{RT}\right) - exp\left(-\frac{(1-\alpha)nF\eta_{act,i}}{RT}\right)\right] \tag{30}$$

Where $J_{o,i}$ is the electrode exchange current density (A/m^2) and α the transfer coefficient (unitless), which is typically set to a value of 0.5. However, here a simplified version was used instead (Equation (31)), as this altered expression has been shown to provide higher accuracy over a range of current densities when α has a value less than or equal to 0.7 [24,25]:

$$\eta_{act,i} = \frac{RT}{F}ln\left[\frac{1E+4\cdot J}{2J_{o,i}} + \sqrt{\left(\frac{1E+4\cdot J}{2J_{o,i}}\right)^2 + 1}\right] \tag{31}$$

The exchange current density represents the local current density that flows at open-circuit voltage and can be described by Equation (32), where γ_i and $E_{a,i}$ are respectively the pre-exponential factor (A/m^2) and activation energy (J/mol) associated with the relevant electrode [26–28]:

$$J_o = \gamma_i exp\left(-\frac{E_{a,i}}{RT}\right) \tag{32}$$

Finally, the quantity of heat required to be provided to the unit by the furnace was found by performing a heat balance across the block, considering the enthalpies of the input/output streams, the enthalpy change associated with the steam decomposition reaction and the heat produced by the electrolyser itself (i.e. the calculated SOE power).

The SEOP sub-section consisted of three SEOPs connected in series, which progressively removed oxygen from a flow of air and thus produced the purified stream of nitrogen required for ammonia synthesis. On each side, compressed air is fed to HE-06 and HE-07, where heat is recuperated from the relevant effluent and the incoming streams thereafter brought up to the operating temperature by an electric heater. The flow of air fed to the cathode-side (stream 41) was controlled such that a 3:1 M ratio of H_2 to N_2 would be achieved in the outlet stream of MIX-02; the anode-side inlet flow (stream 49) was set to achieve a certain oxygen mole fraction in the exhaust as was the case for the SOE model. The purified nitrogen produced on the cathode-side of the SEOP series (stream 48) was combined with the H_2 produced in the SOE whilst the anode-side output (stream 56) was simply vented to the atmosphere.

As the operating principle is so similar to that of an SOE, each SEOP was also modelled using a Python script model. The material balance on each side of the cell was completed by computing the molar flowrate of O_2 oxidised or produced at the electrodes $\dot{n}_{O_2}$ (mol/s) using the basic electrolysis equation shown in Equation (33):

$$\dot{n}_{O_2} = \frac{JA}{nF} \tag{33}$$

The Nernst potential was calculated using Equation (10) and the operating voltage, overpotentials and power consumption found using the same manner as for the SOE model. In this case, the heat balance was used to find the temperature of the output streams; it was assumed that thermal equilibrium was reached across each unit and so both streams exited at the same temperature. Note that no external heat was provided to any of the SEOPs.

To properly simulate a cryogenic Air Separation Unit, a complicated model with multiple distillation columns, heat exchangers and compressors/expanders would be required. However, to reduce the number of components and thus simplify the model, it was decided to represent the ASU using a single compound separator with the inlet flow of air adjusted such that a 3:1 H_2 to N_2 molar ratio would be achieved in the output stream of MIX-02. The nitrogen purity was set to 99.45 mol% and the energy consumption of the unit set to 200 kWh per tonne of separated O_2 (calculated from stream 42), a value taken from the literature [29].

Whilst it would have been preferable to model the Haber-Bosch Reactor using equilibrium calculations, for improved convergence it was decided to instead model this using a Python script as a conversion reactor operating isothermally at 400 °C and 150 bar. The reactor was considered to operate at thermodynamic equilibrium and the N_2 conversion was assumed to be fixed at 30%, a value taken from the open literature [15].

Several parameters were defined to allow the performance of sub-sections or the systems as a whole to be assessed.

The efficiency of the SOE sub-section η_{SOE} was calculated by dividing the enthalpy of the product H_2 (on a lower heating basis) by the required input energy, in accordance with Equation (34):

$$\eta_{SOE} = \left(\frac{\dot{m}_{H_2}LHV_{H_2}}{P_{in}}\right)\cdot 100\% \tag{34}$$

Where $\dot{m}_{H_2}$ is the mass flowrate of hydrogen produced by the electrolyser (kg/s), LHV_{H_2} is the lower heating value of said hydrogen (MJ/kg) and P_{in} the electrical power consumed by the SOE sub-section (kW).

Similarly, the global efficiency η_{system} was found by dividing the enthalpy of the ammonia produced by the system by the consumed energy as shown by Equation (35):

$$\eta_{system} = \left(\frac{\dot{m}_{NH_3} LHV_{NH_3}}{P_{in}} \right) \cdot 100\% \quad (35)$$

where $\dot{m}_{NH_3}$ (kg/s) and LHV_{NH_3} (MJ/kg) are the mass flowrate and lower heating value of ammonia respectively.

The specific energy consumption of the three individual sub-sections or the complete systems was quantified in kWh/kgNH_3 using Equation (36):

$$Specific\ \ Energy\ \ Consumption = \frac{P_{in}}{\dot{m}_{NH_3}} \quad (36)$$

An outline of the terms included in the calculation of P_{in} for the three sub-sections and the complete systems is presented in Table SM 1 of the attached supplementary material.

3. Results and discussion

To ensure the results obtained from the full case A system model were valid, the SEOP-01 model was first run in isolation using the input parameters listed in Table SM 2 of the attached supplementary material. Fig. 6 shows some results obtained from these simulations. The SEOP cell voltage increased as the applied current density rose as expected whilst the molar fraction of oxygen in the cathode-side product stream decreased, Fig. 6A. Furthermore, the cell voltages were comparable to those found in the literature [20,21] which added credibility to the model. Despite the fact that the flowrate of sweep air required to maintain an oxygen molar fraction of 0.22 in the anode exhaust increased with J, the device always operated in an exothermic space with the temperature of the outputs rising marginally over the studied range (Fig. 6B). This was a result of the aforementioned trend in the cell voltage and also the lack of a net endothermic reaction taking place in the unit. From a system design perspective, this is a useful characteristic as it means that in addition to allowing for the separation of O_2 from multi-component gaseous mixtures, the SEOP could also be used as a heat source. The Nernst potential was −0.0010 V, which indicated that oxygen could flow from cathode to anode spontaneously without any external electrical input i.e. the pressure gradient across the cell alone was a sufficient driving force to affect separation. Mathematically, this negative E_{REV} can be explained by the fact that the cathode and anode input pressures of 1.3 and 1.25 bar respectively forced the logarithmic term of Equation (10) to achieve a negative value. At an applied current density of 0.0014 A/cm^2, the five calculated overpotentials were all small enough to allow for the cell voltage to maintain a negative value of −0.0006 V (Table 1). The activation losses accounted for the vast majority of the total overpotential as expected at such a current flow. Additionally, the concentration overpotentials are worthy of note as the returned values indicated that the partial pressure of O_2 at the reaction sites was only slightly different to the bulk on each side of the cell.

Table 2 presents the results of each system case in terms of model inputs and outputs. A list of input parameters specific to case A and case B are shown in Table SM 3 and Table SM 4 whilst Table SM 5 and Table SM 6 give inputs common to both systems. The SOE and SEOP inputs were taken from [28,30]; results obtained from simulations performed by the authors at 689–1000 °C using these parameters agreed well with the experimental results of [28,31]. At an applied current density of 0.35 A/cm^2, the SOE produced 4.35 mol/s of hydrogen in each case. The calculated cell voltage was 0.876 V, smaller than the thermoneutral voltage of 1.290 V at 900 °C. Therefore, the electrolyser would have operated in a significantly endothermic space had 378.42 kW of heat not been provided to it by the furnace. As a whole, the SOE sub-section consumed 1432.65 kW of electrical energy and as such operated with an efficiency of 73.52%. The vast majority of the energy input to this sub-section was consumed by the SOE itself, i.e. the sum of the electrical power consumed by the unit and the heat provided by the furnace, (1114.18 kW; 77.77%), although the need to raise a significant quantity of steam *via* electrical heating meant that HEATER-01 also incurred a significant (138.80 kW; 9.69%) energy penalty. Additionally, the large flowrate of sweep air (32.21 mol/s) required to achieve an oxygen molar fraction of 0.26 in the SOE anode exhaust also necessitated a large amount of energy (110.65 kW; 7.72%) be expended to

Table 1
The calculated values of the Nernst potential, each of the five overpotentials and the cell voltage of SEOP-01 for an applied current density of 0.0014 A/cm^2.

Parameter	Value
E_{REV} (V)	−0.0010
η_{ohmic} (V)	0.00003
$\eta_{conc,c}$ (V)	0.00001
$\eta_{conc,a}$ (V)	0.00001
$\eta_{act,c}$ (V)	0.00022
$\eta_{act,a}$ (V)	0.00008
V (V)	−0.0006

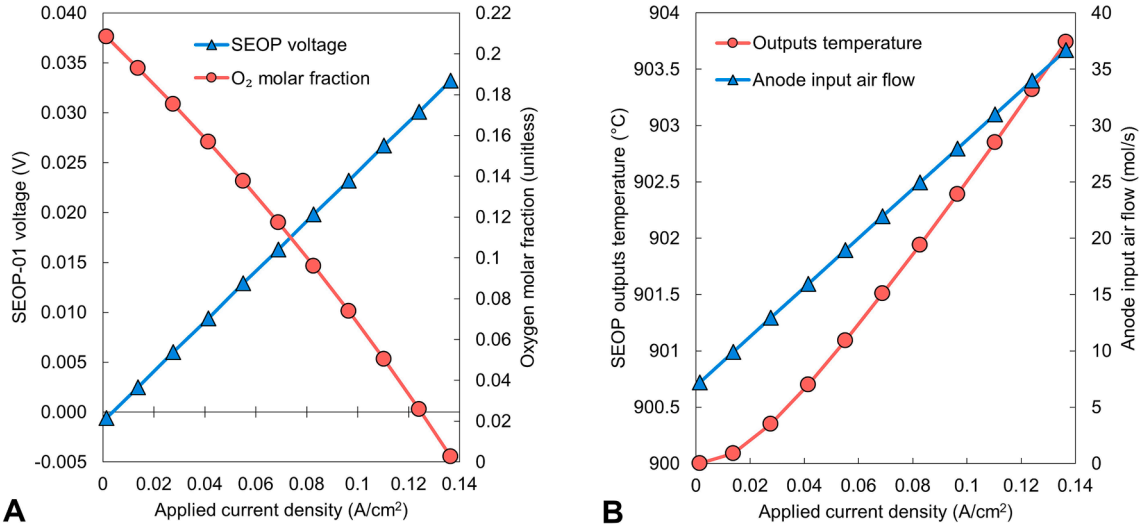

Fig. 6. The variation of (A) cell voltage and O_2 molar fraction in the cathode-side product stream and (B) the outputs temperature and required flowrate of sweep air plotted as a function of the current density applied to SEOP-01.

Table 2
Summary of system performance for case A (SEOP) and case B (ASU) in terms of plant inputs and outputs.

Parameter	Case A	Case B
Plant Inputs		
Power in (kW)	1807.35	1609.13
Water in (mol/s)	6.22	6.22
Air in (mol/s)	63.52	34.05
Power use distribution		
SOE sub-section (kW)	1432.65	1432.65
N_2 production sub-section (kW)	202.82	8.71
Haber-Bosch sub-section (kW)	171.88	167.77
Plant outputs		
SOE voltage (V)	0.876	0.876
Heat provided by Furnace (kW)	378.42	378.42
SOE product H_2 flow (mol/s)	4.35	4.35
SOE product H_2 purity (mol%)	97.14	97.14
Product H_2 heating value (kW)	1053.28	1053.28
N_2 flow to Haber-Bosch (mol/s)	1.45	1.45
N_2 stream purity (mol%)	99.45	99.45
HBR heat duty (kW)	−158.25	−158.25
Steam raised from HBR (mol/s)	2.97	2.97
Product NH_3 flow (mol/s)	2.68	2.68
Product NH_3 flow (g/s)	45.64	45.64
Product NH_3 purity (mol%)	94.53	94.53
Product NH_3 heating value (kW)	851.09	851.09
η_{SOE}(%)	73.52	73.52
η_{system}(%)	47.09	52.89
Specific Energy Consumption (kWh/kgNH_3)	11.00	9.79

condition stream 15 to the SOE operating conditions of 1.2 bar and 900 °C. Whilst there was capacity for reducing the energy demand of this sub-section, optimisation of the system was beyond the scope of this study and so this was not investigated.

Both models were operated in such a manner that the composition of the H_2/N_2 gas mixture fed to the HBL (i.e. stream 28) was normalised, this was accomplished by ensuring that the overall extent of oxygen separation realised by the SEOPs matched that of the ASU. Table 3 demonstrates that SEOP-01 was responsible for the majority of oxygen separation and as a result consumed the most electrical power, with the subsequent units only acting to increase the nitrogen purity of the cathode-side product stream from 93.77 to 99.45 mol%. Even so, SEOP-03 required the largest voltage (0.1075 V) due to the small oxygen partial pressure on the cathode-side of the cell engendering a relatively large Nernst potential. As an aside, an alternative model was constructed in which SEOP-01 alone was deployed. Although it was possible to achieve this high nitrogen purity in a single stage, the unit had to operate with an oxygen separation factor (i.e. the fraction of oxygen gas removed from the cathode-side input stream) of 0.979, likely higher than could be achieved practically. As a result of the normalisation of stream 28, each system produced 45.64 g/s of ammonia. Additionally, in both cases 158.25 kW of waste heat had to be removed from the Haber-Bosch Reactor, which allowed for 2.97 mol/s of steam to be raised from the ammonia reactor or about 48% of the total requirement (6.22 mol/s) of the SOE.

In case A, 1807.35 kW of energy was consumed by the system and so an energetic efficiency of 47.09% and a specific energy consumption of 11.00 kWh/kgNH_3 were achieved. This corresponded to a specific energy consumption of 39.60 GJ/tonneNH_3. While this was of the same order of magnitude, it was significantly larger than several ammonia plants currently in operation, which consume between 28 and 33 GJ per metric tonne of ammonia [32]. Conversely, case B only consumed 1609.13 kW of electrical power and thus achieved an energetic efficiency of 52.89% and a specific energy consumption of 9.79 kWh/kgNH_3 (35.24 GJ/tonneNH_3). This disparity between the two cases can be accounted for by examining the distribution of the specific energy consumption of each plant across the three sub-sections, Fig. 7. Whilst the energy consumed by the SOE sub-section was identical over the two cases as expected, the energy penalty for preparation of the nitrogen stream was over twenty-four times larger in case A (1.23 kWh/kgNH_3) than in case B (0.05 kWh/kgNH_3). Note that the slightly greater consumption of the Haber-Bosch sub-section in case A was due to a higher output temperature of MIX-02 (73 °C compared to 23 °C as in case B), which in turn lead to a small rise in the energy demand of the multistage compression train. Of the energy consumed by the SEOP sub-section 98% was used in either the heating or compression of the two feed streams, Fig. 8. The anode-side feed in particular consumed a large amount of energy due to the high flowrate of air that had to be fed to the unit to achieve an oxygen molar fraction of 0.22 in the anode exhaust. Consequently, the operating envelope of the SEOP sub-section was investigated in an effort to reduce its specific energy consumption and thus bring the efficiency of the novel system closer to that of the reference system.

In the first instance, the flowrate of sweep air was varied such that the oxygen molar fraction in stream 55 would achieve values between 0.22 and 0.30. Fig. 9 demonstrates that this action lead to a substantial reduction in the specific energy consumption of the sub-section, falling from 1.23 kWh/kgNH_3 to 0.24 kWh/kgNH_3 over the studied range. The main driver of this trend was obviously the reduced energy demand for conditioning of the anode-side feed, although a small reduction in the energy required for heating of the cathode-side feed was also observed as a result of the stack operating progressively more exothermically. For example, the output streams of SEOP-01 increased in temperature from 903 °C to 918 °C as the O_2 molar fraction rose from 0.22 to 0.30. No variation in the energy consumption of the other sub-sections was observed (Table SM 7). Therefore, over the investigated range the specific energy consumption of the system decreased from 11.00 kWh/kgNH_3 to 10.01 kWh/ kgNH_3 and thus a substantial increase in η_{system} from 47.09% to 51.77% was observed. This result makes it clear that, like the SOE, the flowrate of sweep air fed to the SEOP is extremely important in determining the efficiency with which the unit will

Table 3
Some results obtained from the series of SEOPs for case A.

Parameter	SEOP-01	SEOP-02	SEOP-03
Applied current density (A/cm^2)	0.1034	0.0776	0.0963
Nernst potential (V)	−0.0010	0.0307	0.0603
Cell voltage (V)	0.0250	0.0519	0.1075
Cathode product N_2 purity (mol%)	93.77	98.04	99.45
Power consumption (kW)	2.79	1.35	0.87

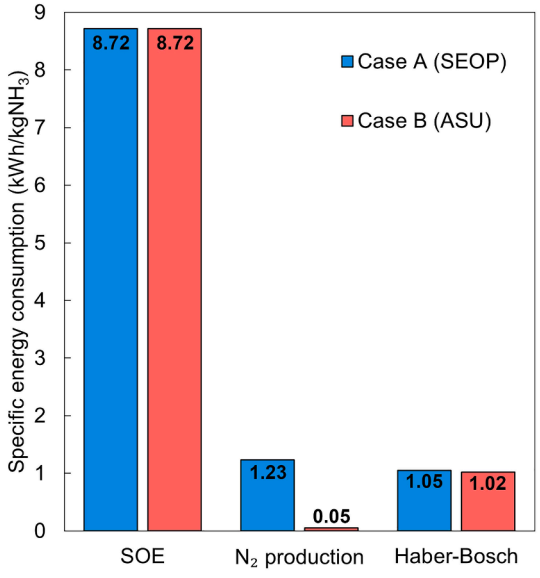

Fig. 7. The distribution of the specific energy consumption (in kWh/kgNH_3) for each system case across the three sub-sections.

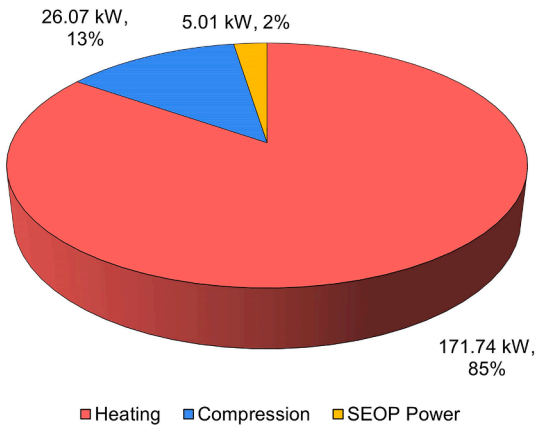

Fig. 8. Assignment of the energy consumption of the SEOP sub-section (case A) between the heating and compression of the two feed streams as well as the electrical power consumed by the SEOPs themselves.

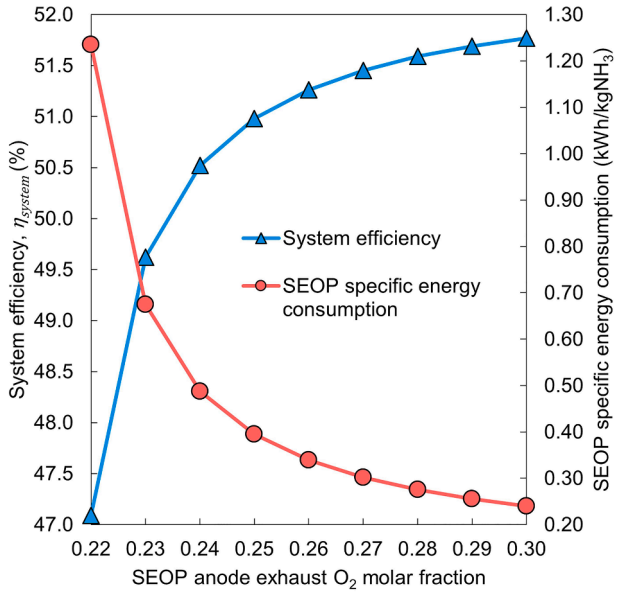

Fig. 9. The variation of the specific energy consumption of the SEOP sub-section and the system efficiency as a function of the molar fraction of oxygen in stream 55. The O_2 molar fraction in this stream was varied by changing the flowrate of sweep air fed to the SEOP series.

operate. However, the presence of a concentrated stream of oxygen at these temperatures obviously undermines the safety case of the plant, particularly if the anode exhaust of the SEOP series were to be in any kind of physical proximity to a hydrogen-containing stream.

With the electrical demand of the SEOPs being directly related to the partial pressure of oxygen on either side of the cell, the cathode-side pressure of SEOP-01 was then varied between 1.3 and 3.0 bar *via* COMP-04 and its effect studied. Fig. 10 shows that the voltage of SEOP-01 decreased by more than 85% over the studied range. Whereas η_{ohmic}, $\eta_{conc,a}$ and the activation overpotentials remained constant, a small reduction in $\eta_{conc,c}$ was observed (Table SM 8) although this was not nearly of a sufficient magnitude. Instead, the reduction in the cell voltage of SEOP-01 was caused by the increasingly large oxygen partial pressure gradient across the cell acting to decrease the Nernst potential from −0.0010 V to −0.0221 V (i.e. the logarithmic term of Equation (10) became more negative with cathode-side pressure). Similar trends were also observed in the voltages of SEOP-02 and SEOP-03. Despite this, the specific energy consumption of the SEOP sub-section actually increased,

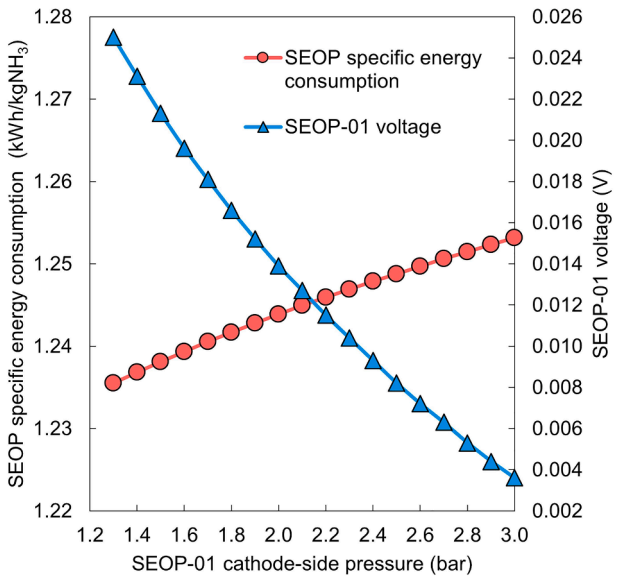

Fig. 10. Trends in the cell voltage of SEOP-01 and the specific energy consumption of the SEOP sub-section with increasing SEOP-01 cathode-side pressure.

caused by the obvious increase in the energy requirement for compression. However, the ejection pressure of MIX-02 rose with increasing cathode pressure and thus a reduction in the energy penalty for compression of the feed gas mixture up to 150 bar was observed. In turn, this reduced the specific energy consumption of the Haber-Bosch sub-section (Table 4) and so brought about a slight improvement in system efficiency from 47.09% to 47.38% as the cathode-side pressure of SEOP-01 rose from 1.3 to 3.0 bar.

It was thus decided to operate the case A model with an SEOP anode exhaust oxygen molar fraction of 0.30 and a pressure of 3.0 bar on the cathode-side of SEOP-01. In this case, an energetic efficiency of 52.12% and a specific energy consumption of 9.94 kWh/kg NH_3 was achieved, very close to the results of the reference case. If an electricity price of £0.30/kWh is assumed this would correspond to an ammonia production cost (excluding capital) of approximately £2.98/kgNH_3. There is still scope however to explore alternate configurations of the SEOP sub-section that could allow for improved integration with the other segments and thus for further improvements in the system efficiency to be realised. For example, in the base case A model, the SEOP anode exhaust (stream 56) exited the system at 244 °C. With the flowrate of sweep air being comparatively large, there is significant enthalpy present in this stream that could be used to e.g. pre-heat the liquid water of stream 6 before it reached HEATER-02. This would enable slightly more steam to be raised using the HBR waste heat and thus reduce the energy demand of HEATER-01. The temperature of stream 56 could be increased by allowing for the temperature of stream 55 to rise by reducing either the active area of one or more of the SEOPs (thus increasing their operating

Table 4
The specific energy consumption of each sub-section and the full case A plant as a function of the cathode-side pressure of SEOP-01. Also shown is the variation in the system efficiency.

	(Sub-)section specific energy consumption (kWh/kgNH$_3$)				
Pressure (bar)	**SOE**	**SEOP**	**Haber-Bosch**	**System**	**η_{system} (%)**
1.3	8.72	1.23	1.05	11.00	47.09
1.5	8.72	1.24	1.03	10.99	47.13
2.0	8.72	1.24	1.01	10.97	47.23
2.5	8.72	1.25	0.98	10.95	47.31
3.0	8.72	1.25	0.96	10.93	47.38

voltages) or the flowrate of sweep air fed to the anode channel. If a sufficiently high grade could be reached, it may even be possible to use stream 56 to raise some of the steam required by the SOE directly, substantially reducing the energy requirement of HEATER-01.

4. Conclusions

To meet net-zero targets, ammonia production must be decarbonised by replacing the conventional approach based on the steam reforming of natural gas. A conceptual design for a green ammonia plant was presented where synthesis was realised *via* a Haber-Bosch loop using hydrogen produced by a solid oxide electrolyser and nitrogen obtained from air using a series of solid electrolyte oxygen pumps. The system operated with an energetic efficiency of 52.12% and a specific energy consumption of 9.94 kWh/kgNH_3. This was similar to a reference case in which the required nitrogen was produced by a cryogenic ASU, where an energetic efficiency of 52.89% and a specific energy consumption of 9.79 kWh/kgNH_3 were achieved. These are encouraging results, but system performance could be increased further through improved heat integration. For example, a portion of the steam demand of the SOE could perhaps be satisfied using the waste heat that flows from the series of oxygen pumps.

CRediT authorship contribution statement

Duncan A. Nowicki: Conceptualization. **Gerry D. Agnew:** Conceptualization. **John T.S. Irvine:** Conceptualization.

Declaration of Competing Interest

The authors declare the following financial interests/personal relationships which may be considered as potential competing interests: John T.S. Irvine reports financial support was provided by Hydrogen and Fuel Cells Hub Extension (H2FC SUPERGEN).

Data availability

Data will be made available on request.

Acknowledgements

The authors gratefully acknowledge financial support from the University of St Andrews and the Hydrogen and Fuel Cells Hub Extension (H2FC SUPERGEN) flexible funding (EP/P024807/1).

John T.S. Irvine reports financial support was provided by Hydrogen and Fuel Cells Hub Extension (H2FC SUPERGEN).

References

[1] IPCC. Climate Change 2014: Synthesis Report. Contribution of Working Groups I, II and III to the Fifth Assessment Report of the Intergovernmental Panel on Climate Change. 2014.
[2] The Royal Society. Ammonia: Zero-Carbon Fertiliser, Fuel and Energy Store Policy Briefing. 2020.
[3] Liu X, Elgowainy A, Wang M. Life Cycle Energy Use and Greenhouse Gas Emissions of Ammonia Production from Renewable Resources and Industrial By-Products. Green Chem 2020;22(17):5751–61.
[4] Xiang D, Zhou Y. Concept Design and Techno-Economic Performance of Hydrogen and Ammonia Co-Generation by Coke-Oven Gas-Pressure Swing Adsorption Integrated with Chemical Looping Hydrogen Process. Appl Energy 2018;229:1024–34.
[5] IPCC. IPCC Special Report on Carbon Dioxide Capture and Storage. Prepared by Working Group III of the Intergovernmental Panel on Climate Change. 2005.
[6] Muthuraj R, Mekonnen T. Recent Progress in Carbon Dioxide (CO_2) as Feedstock for Sustainable Materials Development: Co-Polymers and Polymer Blends. Polymer 2018;145:348–73.
[7] Nowicki DA, Skakle JMS, Gibson IR. Potassium-Carbonate Co-substituted Hydroxyapatite Compositions: Maximising the Level of Carbonate Uptake for Potential CO_2 Utilisation Options. Materials. Advances 2022.
[8] Morrison J, Jauffret G, Galvez-Martos JL, Glasser FP. Magnesium-Based Cements for CO_2 Capture and Utilisation. Cem Concr Res 2016;85:183–91.
[9] Ogden JM. Review of Small Stationary Reformers for Hydrogen Production. Report to the International Energy Agency 2001.
[10] Noussan M, Raimondi PP, Scita R, Hafner M. The Role of Green and Blue Hydrogen in the Energy Transition- A Technological and Geopolitical Perspective. Sustainability 2021;13(1):298.
[11] Holladay JD, Hu J, King DL, Wang Y. An Overview of Hydrogen Production Technologies. Catal Today 2009;139(4):244–60.
[12] Nikolaidis P, Poullikkas A. A Comparative Overview of Hydrogen Production Processes. Renew Sustain Energy Rev 2017;67:597–611.
[13] Frattini D, Cinti G, Bidini G, Desideri U, Cioffi R, Jannelli E. A System Approach in Energy Evaluation of Different Renewable Energies Sources Integration in Ammonia Production Plants. Renew Energy 2016;99:472–82.
[14] Cinti G, Frattini D, Jannelli E, Desideri U, Bidini G. Coupling Solid Oxide Electrolyser (SOE) and Ammonia Production Plant. Appl Energy 2017;192:466–76.
[15] Cheema II, Krewer U. Operating Envelope of Haber-Bosch Process Design for Power-to-Ammonia. RSC Adv 2018;8(61):34926–36.
[16] Klerke A, Christensen CH, Nørskov JK, Vegge T. Ammonia for Hydrogen Storage: Challenges and Opportunities. J Mater Chem 2008;18(20):2304–10.
[17] Krilova AV, Nefedova NV, Peev TM. Poisoning and Passivation of Ammonia Synthesis Catalyst at Various Temperatures. Studies in Surface Science and Catalysis: Elsevier 1987:625–37.
[18] Wang L, Pérez-Fortes M, Madi H, Diethelm S, Maréchal F. Optimal Design of Solid-Oxide Electrolyzer Based Power-to-Methane Systems: A Comprehensive Comparison Between Steam Electrolysis and Co-Electrolysis. Appl Energy 2018;211:1060–79.
[19] Acar C, Dincer I. 3.1 Hydrogen Production. In: Comprehensive Energy Systems. Oxford: Elsevier; 2018. p. 1–40.
[20] Spirin A, Lipilin A, Ivanov V, Paranin S, Nikonov A, Khrustov V, et al. Solid oxide electrolyte based oxygen pump. Adv Sci Technol 2010;65:257–62.
[21] Iora P, Chiesa P, Campanari S. Comparison of Pressure Driven Electrolytic Membranes (PDEM) and Solid Electrolyte Oxygen Pumps (SEOP) for Small Scale Oxygen Production. Energy Procedia 2014;61:639–42.
[22] Cinti G, Bidini G, Hemmes K. An experimental investigation of fuel assisted electrolysis as a function of fuel and reactant utilization. Int J Hydrogen Energy 2016;41(28):11857–67.
[23] Cinti G, Baldinelli A, Di Michele A, Desideri U. Integration of Solid Oxide Electrolyzer and Fischer-Tropsch: A Sustainable Pathway for Synthetic Fuel. Appl Energy 2016;162:308–20.
[24] Ni M, Leung MKH, Leung DYC. Energy and exergy analysis of hydrogen production by solid oxide steam electrolyzer plant. Int J Hydrogen Energy 2007;32(18):4648–60.
[25] Noren DA, Hoffman MA. Clarifying the Butler–Volmer Equation and Related Approximations for Calculating Activation Losses in Solid Oxide Fuel Cell Models. J Power Sources 2005 1 December 2005;152:175-181.
[26] Ni M, Leung MKH, Leung DYC. Parametric Study of Solid Oxide Fuel Cell Performance. Energ Conver Manage 2007;48(5):1525–35.
[27] Ni M, Leung MKH, Leung DYC. Parametric Study of Solid Oxide Steam Electrolyzer for Hydrogen Production. Int J Hydrogen Energy 2007;32(13):2305–13.
[28] Costamagna P, Selimovic A, Del Borghi M, Agnew GDA. Electrochemical Model of the Integrated Planar Solid Oxide Fuel Cell (IP-SOFC). Chem Eng J 2004;102(1):61–9.
[29] Darde A, Prabhakar R, Tranier J, Perrin N. Air Separation and Flue Gas Compression and Purification Units for Oxy-Coal Combustion Systems. Energy Procedia 2009;1(1):527–34.
[30] Patcharavorachot Y, Thongdee S, Saebea D, Authayanun S, Arpornwichanop A. Performance Comparison of Solid Oxide Steam Electrolysis Cells With/Without the Addition of Methane. Energ Conver Manage 2016;120:274–86.
[31] Momma A, Kaga Y, Takano K, Nozaki K, Negishi A, Kato K, et al. Experimental Investigation of Anodic Gaseous Concentration of a Practical Seal-Less Solid Oxide Fuel Cell. J Power Sources 2005;145(2):169–77.
[32] Brightling J. Ammonia and the Fertiliser Industry: The Development of Ammonia at Billingham. Johnson Matthey Technol Rev 2018;62(1):32–47.
[33] Zhang H, Wang L, Maréchal F, Desideri U. Techno-Economic Comparison of Green Ammonia Production Processes. Appl Energy 2020;259:114135.